International Journal of Heat and Mass Transfer 112 (2017) 891–902

Contents lists available at ScienceDirect

International Journal of Heat and Mass Transfer

journal homepage: www.elsevier.com/locate/ijhmt

Analytical modeling of liquid saturation jump effect for hydrogen alkaline anion exchange membrane fuel cell

Sen Huo [a], Jae Wan Park [b,*], Pu He [a], Dawei Wang [a], Kui Jiao [a,*]

[a] Tianjin University, 135 Yaguan Rd, Tianjin 300350, China
[b] Department of Mechanical and Aerospace Engineering, University of California, One Shields Ave., Davis, CA 95618, USA

ARTICLE INFO

Article history:
Received 24 December 2016
Accepted 29 April 2017
Available online 17 May 2017

Keywords:
Alkaline anion exchange membrane fuel cell
Analytical model
Water management
Pressure continuity
Liquid saturation jump

ABSTRACT

Alkaline anion exchange membrane fuel cell (AEMFC) has been recognized as a promising zero-emission power source for portable, mobile and stationary application in recent years. To ensure high ionic conductivity and efficient reactants delivery, water management is regarded as one of the most critical issues for AEMFC. In this study, an analytical model is formulated to investigate the effect of electrode wettability on the water transport and resultant AEMFC performance. The pressure continuity method is considered to simulate liquid saturation jump on the interfaces of adjacent electrode layers. The results show that decreasing the cathode catalyst layer (CL) contact angle improves the performance because more water can be kept in the cathode CL decreasing polarization losses. The anode micro porous layer (MPL) is generally helpful, by forcing the liquid water to back-diffuse to the cathode. However, cathode MPL hinders the water transport to the cathode CL, leading to a lower reaction rate and membrane conductivity. The liquid water injection into the cathode has great potential to further improve the performance of AEMFC, however it may cause flooding in the flow channel and GDL. The cathode reaction kinetics should be considered as one of the most significant factors dragging the cell performance.

1. Introduction

Along with the rapid development of the proton exchange membrane fuel cell (PEMFC) technology [1,2], alkaline anion exchange membrane fuel cell (AEMFC) has also attracted considerable attention over last few decades [3]. AEMFCs, which directly convert chemical energy of fuel and oxidant to electricity in the alkaline environment, have been regarded as clean and efficient power sources for various applications including power plants, zero/low emission vehicles [4], combined heat and power (CHP) systems [5] and aerospace power systems [6].

Although PEMFC exhibits remarkable thermal and mechanical stability, as well as high ionic conductivity, several prominent disadvantages have been presented which preclude its commercialization, including slow electrochemical kinetics, carbon monoxide poisoning of precious Pt-based catalysts, and the high cost of polymer membranes. Compared with PEMFC, AEMFC has several advantages, such as environmentally friendly alkaline chemistry with fast electrochemical reaction and potential uses of non-precious-metals-based catalysts which is critically important for the cost reduction and commercial development. Since the development of the AEMFC is still in its early stage, the researches mainly focus on two aspects, preparation of high performance ionic membrane and non-precious electrode catalysts.

In recent years, several high performance alkaline membranes have been developed for AEMFCs. Li and Zhao measured the water uptake and transport properties of an alkaline membrane (A201 membrane from Tokuyama Corporation, Japan) [7]. The water uptake, ionic conductivity (hydroxide ions (OH^-)) and swelling properties were also measured for the same membrane by Duan et al. [8]. The membranes developed by Tuan et al. [9] aminated with the trimethylamine (PAEK-TMA), triethylamine (PAEK-TEA), tripropylamine (PAEK-TPA) has ionic conductivities up to 0.014, 0.003, and 0.0008 S cm^{-1} at 40 °C and 0.021, 0.006, and 0.0014 S cm^{-1} at 80 °C, respectively. Lin et al. [10] synthesized an imidazolium-based cross-linked AEM that has ionic conductivity up to 0.02 S cm^{-1} with long-term chemical stability in 1 M KOH solution. The studies for alkaline membrane greatly facilitate the rising of the AEMFC.

On the other hand, a wider variety of catalysts utilizing non-precious metals and metal-free materials have been developed and demonstrated in the alkaline environment. Kruusenberg et al. developed a catalyst using Co and Fe phthalocyanine and reported that the performance was slightly inferior to the commercial Pt/C catalysts [11]. Li et al. carried out cell performance tests

* Corresponding authors.
E-mail address: kjiao@tju.edu.cn (K. Jiao).

http://dx.doi.org/10.1016/j.ijheatmasstransfer.2017.04.137
0017-9310/

using non-precious catalysts synthesized from precursors of carbon, nitrogen, and transition metals. They reported a maximum power density of 177 mW cm^{-2} at 50 °C [12]. Other catalysts, such as carbon-supported non-platinum materials, were also developed for hydrogen and methanol AEMFCs exhibiting excellent performances [13,14].

Similar to PEMFC, water management is also an important issue which is definitely worth exploring [15,16]. However, in the most of the previous researches in the literature, the water management, which actually plays a pivotal role in maintaining and promoting AEMFC performance, has been generally ignored. So far, only a small number of numerical modeling and experimental works have been conducted to investigate the characteristics of water transport in AEMFC [17–26]. It should be noticed that the heat and mass transfer characteristics, such as the liquid water saturation jump effect at the interfaces of the cell components, still need further investigation. Therefore, this study can be viewed as an important supplement to the literature, which mainly focuses on the development of a complete analytical model for AEMFC with consideration of the saturation jump effect. Fig. 1a illustrates the operation of a hydrogen AEMFC with micro-porous layer (MPL). Water is produced in the anode catalyst layer (CL) and consumed in the cathode CL. Water should be removed from the anode while humidification is necessary for the cathode. It should be noticed that liquid saturation jump on the interfaces of different layers (CL/MPL, MPL/GDL) should be taken into consideration due to the different porosity, permeability and wettability on the neighboring layers. To optimize the water transport between anode and cathode, the MPL has been widely used in PEMFCs, and approved to be an effective way to improve the performance [27–31], by affecting mass transport and water removal. Liquid water breakthrough was observed in the MPL of a PEMFC using synchrotron X-ray radiography [27]. The electrical and thermal conductivity of MPL was calculated through a phase-differentiated model [28]. Two main functions of MPL in PEMFC, reducing the water droplet size and blocking the liquid water breakthrough toward GDL, were discussed [29]. Chen et al. also pointed out that MPL could prevent water flooding at low operating temperature and high inlet humidification, and also enhance the membrane thermal and electrical performance under dry condition [30]. Tabe et al. also proposed that MPL could help mitigate the water flooding problem under normal operation, and even improve the cold start performance [31]. The similar mechanisms can be applied to AEMFCs however the effect of MPL and electrode wettability has been generally ignored in previous studies. In addition, most of the previous modeling studies assumed continuous liquid concentration at the interfaces between the neighboring layers and the liquid concentration jump caused by the different physical properties of both sides are neglected.

In this work, an analytical model has been developed for a hydrogen AEMFC to investigate the effect of the MPL and the electrode wettability on water transport. The liquid saturation jump is all considered using pressure continuous method. Experimental testing was also carried out for results comparison. The model formulation and experimental conditions are described in the following sections.

2. Model formulation

As shown in Fig. 1, humidified hydrogen (H_2) and air are supplied for the AEMFC operation. Water back diffusion, electro-osmotic drag and water production all occur during operation, which is similar to PEMFC. However, the direction of electro-osmotic drag of AEMFC is opposite to PEMFC; the water production is in anode for AEMFC but cathode for PEMFC; and water is even consumed in AEMFC cathode. These differences may also result in different water back diffusion directions. The oxygen (O_2) and water is consumed in the cathode generating OH^-, and OH^- move through the ionomer membrane to the anode where the H_2 reacts with OH^- to generate water and electrons (e^-). The e^- transfers through the external circuit to the cathode. Specifically, water is produced at the anode and consumed at the cathode. The electro-osmosis drag effect moves water from the cathode to the anode, and due to the concentration gradient, water can also diffuse back from the anode to the cathode through the membrane.

In this model, the cell output voltage is calculated from reversible voltage, activation overpotentials of anode and cathode, and ohmic overpotentials of the cell components. Reactants are assumed to be ideal gases and their transports are analyzed to calculate the overpotentials. The modeling parameters are listed in Table 1. The mass balance equations of liquid water and gas species are listed in Tables 2 and 3, respectively.

2.1. Modeling assumptions

(1) Due to the low Reynolds number, the flow is assumed to be laminar and in steady state.
(2) The gases follow the ideal gas law.
(3) The model is assumed to be isothermal due to the small cell size and low reaction rate (low current density).
(4) To simplify the calculation in water phase change, it is assumed that if the local water vapor is saturated, the product water is in liquid form, and otherwise, it is in vapor form.
(5) The gas pressure is assumed to be 1 atm and evenly distributed in the fuel cell.
(6) The membrane is assumed to be impermeable to the gas phase.

2.2. Output voltage

The cell output voltage, E_{out} (V), is calculated as

$$E_{out} = E_{rev} - \eta_{ohm} - \eta_{act} \tag{1}$$

where E_{rev} (V) is the reversible cell potential, η_{ohm} (V) is the ohmic overpotential, and η_{act} (V) is the activation overpotential. Based on the Nernst equation [32], the reversible cell potential can be expressed as

$$E_{rev} = 1.229 - 0.846 \times 10^{-3}(T - T_{ref}) + \frac{RT}{2F}\left(\ln p_{H_2,ano} + \frac{1}{2}\ln p_{O_2,cat}\right) \tag{2}$$

where T is the operating temperature (K), T_{ref} is the reference temperature (298.15 K). F is the Faraday's constant (96,487 C mol^{-1}), R is the universal gas constant (8.314 J mol^{-1} K^{-1}), and $p_{H_2,ano}$ and $p_{O_2,cat}$ (atm) are the partial pressures of the H_2 and O_2 at the inlets. Note that this equation is for water production in liquid form, and the partial pressures are divided by a standard pressure of 1 atm.

2.3. Ohmic overpotential

Ohmic resistances are taken into consideration in the membrane, porous media, and flow field plate. The ohmic overpotential, η_{ohm} (V), is expressed as follows:

$$\eta_{ohm} = \eta_{ohm,P} + \eta_{ohm,por} + \eta_{ohm,m} = (R_{e^--P} + R_{e^--por} + R_{OH^--por} + R_{OH^--m}) \times I \tag{3}$$

where I (A m^{-2}) is the current density. $\eta_{ohm,P}$, $\eta_{ohm,por}$ and $\eta_{ohm,m}$ (V) denote the ohmic overpotential of the bipolar plate, porous media

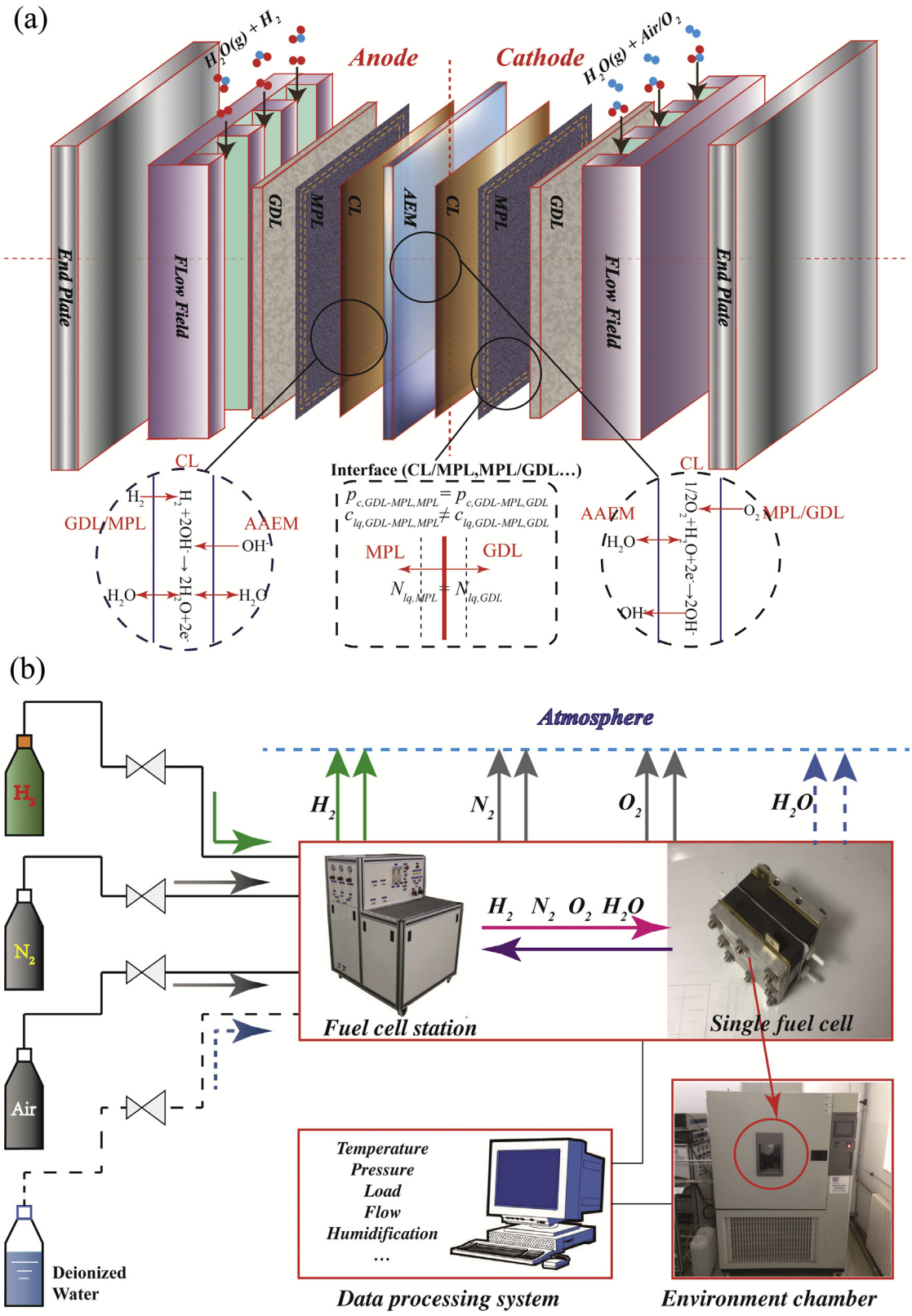

Fig. 1. Schematics of (a) an alkaline anion exchange membrane fuel cell (AEMFC) with micro-porous layers (MPL), and (b) the experimental setup.

(including the GDL, MPL and CL) and membrane, respectively. The ohmic resistance is comprised of the electron transport in the bipolar plate ($R_{e^-\_P}$, $\Omega\,m^2$), GDL, MPL and CL ($R_{e^-\_por}$, $\Omega\,m^2$) and the OH^- transport in the electrolyte in CL ($R_{OH^-\_por}$, $\Omega\,m^2$) and AEM ($R_{OH^-\_m}$, $\Omega\,m^2$). For simplification, the OH^- and electron are assumed to be consumed/produced at the middle site of the CL. The effective electrical conductivities of OH^- and electron, σ_m^{eff} and σ_s^{eff} ($S\,m^{-1}$), in the porous media (GDL, MPL and CL), are determined

Table 1
Modeling parameters for base operating condition.

Parameter	Value	Unit
Operating temperature (inlet temperature), T	50	°C
Operating pressure, p_{opt}	1.0	atm
Global stoichiometry ratio of reactants, ST	2.0	
Relative humidity of anode inlet gases, RH_{ano}	100%	
Relative humidity of cathode inlet gases, RH_{cat}	100%	
Thickness of GDL, MPL,CL, δ_{GDL};δ_{MPL};δ_{CL};	200; 30;10	μm
Thickness of AEM, δ_m	28	μm
Porosity of electrodes, ε_{GDL}; ε_{MPL}; ε_{CL}	0.6;0.4;0.3	
Contact angles of electrodes, θ_{GDL};θ_{MPL};θ_{CL}	100;120;100	°
Channel dimension (length, width, depth), L;W;D	100;1.0;1.0	mm
Resistivity of electrode; flow channel plate, $\rho_{ohm,por}$; $\rho_{ohm,P}$	6×10^{-5};6×10^{-5}	Ω m
Intrinsic permeability of GDL, MPL, CL, $K_{0,GDL}$;$K_{0,MPL}$;$K_{0,CL}$	6.2×10^{-12};1.5×10^{-12};6.2×10^{-13}	m^2
Reference current density at anode, $J^{ano}_{0,ref}$	$5\times10^{6}\cdot\exp\left[-1400\cdot\left(\frac{1}{T}-\frac{1}{353.15}\right)\right]$	A m^{-3}
Reference current density at cathode, $J^{cat}_{0,ref}$	$10\cdot\exp\left[-7900\cdot\left(\frac{1}{T}-\frac{1}{353.15}\right)\right]$	A m^{-3}
Evaporation, condensation rates, γ_{evap}; γ_{cond}	1	s^{-1}

Table 2
Mass balance equations for liquid water.

Mass balance equation	Solved in
$\frac{\left(c^{lq,ano}_{GDL-MPL,GDL}-c^{lq,ano}_{ch-GDL}\right)D_{lq,GDL,ano}}{\delta_{GDL}}=N_{ano,lq}$	Anode GDL
$\frac{\left(c^{lq,ano}_{MPL-CL,MPL}-c^{lq,ano}_{GDL-MPL,MPL}\right)D_{lq,MPL,ano}}{\delta_{MPL}}=N_{ano,lq}$	Anode MPL (if exists)
$\frac{M_{H_2O}I}{F\delta_{CL}}+\frac{n_dM_{H_2O}I_{cat,lq}}{F\delta_{CL}}=\frac{D_m(\rho_{w-a}-\rho_{w-c})}{\delta_m\delta_{CL}}+\frac{N_{ano,lq}M_{H_2O}}{\delta_{CL}}$ $\frac{\left(c^{lq,ano}_{CL-AAEM}-c^{lq,ano}_{MPL-CL,CL}\right)D_{lq,CL,ano}}{\delta_{CL}}=N_{ano,lq}$	Anode CL
$\frac{M_{H_2O}I_{cat,lq}}{2F\delta_{CL}}+\frac{n_dM_{H_2O}I_{cat,lq}}{F\delta_{CL}}+\frac{N_{cat,lq}M_{H_2O}}{\delta_{CL}}=\frac{D_m(\rho_{w-a}-\rho_{w-c})}{\delta_m\delta_{CL}}$ $\frac{\left(c^{lq,cat}_{CL-AAEM}-c^{lq,cat}_{MPL-CL,CL}\right)D_{lq,CL,cat}}{\delta_{CL}}+S_{vap-lq,CL}\delta_{CL}=N_{cat,lq}$	Cathode CL
$\frac{\left(c^{lq,cat}_{MPL-CL,MPL}-c^{lq,cat}_{GDL-MPL,MPL}\right)D_{lq,MPL,cat}}{\delta_{MPL}}+S_{vap-lq,MPL}\delta_{MPL}=N_{cat,lq}$	Cathode MPL (if exists)
$\frac{\left(c^{lq,cat}_{GDL-MPL,GDL}-c^{lq,cat}_{ch-GDL,GDL}\right)D_{lq,GDL,cat}}{\delta_{GDL}}+S_{vap-lq,GDL}\delta_{GDL}=N_{cat,lq}$	Cathode GDL

by the Bruggeman's correlation ($\sigma^{eff}_i=\sigma^0_i\cdot\Theta^{1.5}, i=m$ and s) [33], based on the intrinsic electrical conductivity, σ^{eff}_m and σ^{eff}_s (S m^{-1}), and the volume fraction of transfer path (Θ). As mentioned above, Duan et al. [8] provided the variation of ionic conductivity of A201 membrane as a function of operating temperature (T, K) and water content (λ) in the membrane. λ is a function of operating temperature and average water activity (a_{ave}) in the membrane and determined based on the following correlation [8]:

$$\lambda=\begin{cases}4.908-0.0153T-(0.205T-87.596)a_{ave}\\ \quad+(0.85T-313.878)a^2_{ave}-(0.48T-189.312)a^3_{ave} & \text{if } 0.0<a_{ave}<1.0\\ (0.05795-0.00265a_{ave})(T-313.15)\\ \quad+14.817+1.5915(a_{ave}-1) & \text{if } 1.0<a_{ave}<3.0\end{cases} \tag{4}$$

Table 3
Mass balance equations for gas species.

Species	Mass balance equation	Solved in
Hydrogen (Anode)	$\frac{\left(c^{H_2}_{ch}-c^{H_2}_{ch-GDL}\right)D_{H_2}A_{ch-GDL}Sh}{d_hWL}=\frac{I}{2F}$	Flow channel
	$\frac{\left(c^{H_2}_{ch-GDL}-c^{H_2}_{GDL-MPL}\right)D^{eff}_{H_2,GDL}}{\delta_{GDL}}=\frac{I}{2F}$	GDL
	$\frac{\left(c^{H_2}_{GDL-MPL}-c^{H_2}_{MPL-CL}\right)D^{eff}_{H_2,MPL}}{\delta_{MPL}}=\frac{I}{2F}$	MPL (if exists)
	$\frac{\left(c^{H_2}_{MPL-CL}-c^{H_2}_{CL-AAEM}\right)D^{eff}_{H_2,CL}}{\delta_{CL}}=\frac{I}{2F}$	CL
Oxygen (Cathode)	$\frac{\left(c^{O_2}_{ch}-c^{O_2}_{ch-GDL}\right)D_{O_2}A_{ch-GDL}Sh}{d_hWL}=\frac{I}{4F}$	Flow channel
	$\frac{\left(c^{O_2}_{ch-GDL}-c^{O_2}_{GDL-MPL}\right)D^{eff}_{O_2,GDL}}{\delta_{GDL}}=\frac{I}{4F}$	GDL
	$\frac{\left(c^{O_2}_{GDL-MPL}-c^{O_2}_{MPL-CL}\right)D^{eff}_{O_2,MPL}}{\delta_{MPL}}=\frac{I}{4F}$	MPL (if exists)
	$\frac{\left(c^{O_2}_{MPL-CL}-c^{O_2}_{CL-AAEM}\right)D^{eff}_{O_2,CL}}{\delta_{CL}}=\frac{I}{4F}$	CL
Water vapor (Cathode)	$\frac{\left(c^{vap}_{ch}-c^{vap}_{ch-GDL}\right)D_{vap}A_{ch-GDL}Sh}{d_hWL}+S_{vap-lq,ch}\frac{1}{2}\delta_{ch}=\frac{I-I_{cat,lq}}{2F}$	Flow channel
	$\frac{\left(c^{vap}_{ch-GDL}-c^{vap}_{GDL-MPL}\right)D^{eff}_{vap,GDL}}{\delta_{GDL}}+S_{vap-lq,GDL}\delta_{GDL}=\frac{I-I_{cat,lq}}{2F}$	GDL
	$\frac{\left(c^{vap}_{GDL-MPL}-c^{vap}_{MPL-CL}\right)D^{eff}_{vap,MPL}}{\delta_{MPL}}+S_{vap-lq,MPL}\delta_{MPL}=\frac{I-I_{cat,lq}}{2F}$	MPL (if exists)
	$\frac{\left(c^{vap}_{MPL-CL}-c^{vap}_{CL-AAEM}\right)D^{eff}_{vap,CL}}{\delta_{CL}}+S_{vap-lq,CL}\delta_{CL}=\frac{I-I_{cat,lq}}{2F}$	CL

where a_{ave} is calculated by averaging the water activity (a) in the anode and cathode CLs, and both the water activities in vapor and liquid phase are considered. Namely, the water activity varies from 0 to 3 (usually greater than 1) in this study. The water activity, a, can be expressed as Eq. (5) [34,35]. Moreover, according to the measurements in [36,37], the results also revealed that the water content is higher when immersing polymer membrane to liquid water than that exposing to saturated vapor.

$$a=\frac{X_{vap}p_g}{p_{sat}}+2s_{lq,CL} \tag{5}$$

The first and second terms on the right hand side represent the water activity in vapor and liquid phase, respectively. X_{vap} denotes the volume fraction of water vapor in gas mixture. p_g and p_{sat} (Pa) represent the partial pressure and saturated vapor pressure. $s_{lq,CL}$ is the liquid water volume fraction in the CL. Note that, according to [8], the water activity in liquid phase is ignored in [8] (i.e. a_{ave} ranges from 0 to 1); however, the liquid water is still considered in Eq. (5) in this study since it is a significant factor of the membrane performance. The electrical conductivity of membrane (σ^0_{mem}, S m^{-1}) is also provided by the experiments from [8] and is fitted to be

$$\begin{aligned}\sigma^0_{mem}=&\,0.1334-3.882\times10^{-4}T+(0.01148T-3.909)a_{ave}\\&-(0.06690T-23.01)a^2_{ave}+(0.1227T-42.61)a^3_{ave}\\&-(0.06021T-21.80)a^4_{ave}\end{aligned} \tag{6}$$

2.4. Activation overpotential

The activation overpotentials at the anode ($\eta_{act,ano}$, V) and cathode ($\eta_{act,cat}$, V) are defined as

$$\eta_{act,ano}=\varphi_m-\varphi_{s,ano} \tag{7}$$

$$\eta_{act,cat}=\varphi_{s,cat}-\varphi_m \tag{8}$$

where φ_s ($\varphi_{s,ano}$ and $\varphi_{s,cat}$,V) and φ_m (V) are the potentials of electron and OH^-, respectively. The charge conservation equations of electron and OH^- in one-dimensional form (through-plane) can be expressed as

$$\text{Electron}: \frac{d^2\varphi_s}{dx^2} = \frac{1}{\sigma_s^{eff}} R_i \tag{9}$$

$$OH^-: \frac{d^2\varphi_m}{dx^2} = -\frac{1}{\sigma_m^{eff}} R_i \tag{10}$$

in which the superscript, *eff*, denotes the effective transport properties based on the Bruggeman's correction. σ_s^{eff} and σ_m^{eff} (S m^{-1}) are the effective electrical conductivities of electron and OH^-, respectively. R_i (A m^{-3}) represents the reaction rate. Eqs. (7)–(10) lead to the relationship between the reaction rate (R_i) and the individual activation overpotential ($\eta_{act,ano}$, $\eta_{act,cat}$, V) in the anode and cathode.

The Butler-Volmer equation also provides the relationship between the activation overpotential (η_{act}) and reaction rate (R_i):

$$R_i = (1 - s_{lq}) J_{0,ref} \left(\frac{c_i}{c_{i,ref}}\right)^{r_i} \left[\exp\left(\frac{\alpha n F}{RT}\eta_{act}\right) - \exp\left(-\frac{\alpha n F}{RT}\eta_{act}\right)\right] \tag{11}$$

where s_{lq} is the liquid water volume fraction which is used to correct the reaction rate.

$J_{0,ref}$ (A m^{-3}) is the reference volumetric current density for the reference concentration of species *i*, $c_{i,ref}$ (mol m^{-3}), c_i (mol m^{-3}) is the superficial molar concentration of reactant *i*, H_2, O_2 and vapor, on the reaction site. α (0.5) is the transfer coefficient of the electrochemical reaction. *n* (anode: 2; cathode: 4) is moles of electron transfer with 1 mol of reactant (H_2 or O_2) consumption in the electrochemical semi-reaction. r_i is the order of the reaction, and η_{act} (V) represents the activation overpotential.

The analytical solutions of anode and cathode activation overpotentials ($\eta_{act,ano}$ and $\eta_{act,cat}$, V) can be derived from Eqs. (7)–(11):

$$\eta_{act,ano} = \frac{RT}{\alpha n F}\cosh^{-1}\left[\frac{I^2}{4\sigma_m^{eff2}\left(\frac{\sigma_m^{eff}+\sigma_s^{eff}}{\sigma_m^{eff}\sigma_s^{eff}}\right)\left(\frac{RT}{\alpha n F}\right)(1-s_{lq})J_{0,ref}^{ano}\left(\frac{c_{H_2}}{c_{H_2,ref}}\right)} + 1\right] \tag{12}$$

$$\eta_{act,cat} = \frac{RT}{\alpha n F}\cosh^{-1}\left[\frac{I^2}{4\sigma_m^{eff2}\left(\frac{\sigma_m^{eff}+\sigma_s^{eff}}{\sigma_m^{eff}\sigma_s^{eff}}\right)\left(\frac{RT}{\alpha n F}\right)(1-s_{lq})J_{0,ref}^{cat}\left(\frac{c_{O_2}}{c_{O_2,ref}}\right)\left(\frac{c_{H_2O}}{c_{H_2O,ref}}\right)} + 1\right] \tag{13}$$

Details of the derivation procedure can be found in our published work [38]. Here, c_{H_2O} (mol m^{-3}) represents the water concentration in cathode CL, including the water in liquid and vapor phases. $J_{0,ref}^{ano}$ and $J_{0,ref}^{cat}$ (A m^{-3}) are the reference volumetric current densities in anode and cathode, respectively, which are related to the operating temperature (*T*), as listed in Table 1. In Eqs. (12) and (13), the activation overpotential is mainly affected by the concentration of H_2, O_2 and water. The reactant transport is crucial not only for the activation overpotential but also for the membrane transport properties and ohmic resistance as described in Eqs. (4)–(6).

2.5. Multiphase transport analysis

The mass conservation equation of liquid water is solved in the GDL, MPL and CL.

$$\nabla\cdot(\rho_{lq}\imath\vec{u}_g) = \nabla\cdot(\rho_{lq}D_{lq}\nabla s_{lq}) + S_{lq} \tag{14}$$

where ρ_{lq} (kg m^{-3}) is the mass density of liquid water. $\imath$ is the interfacial drag coefficient. $\vec{u}_g$ (m s^{-1}) is the flow velocity of gas mixtures in the porous media. D_{lq} (m^2 s^{-1}) is the capillary diffusivity of liquid water in the pores of cell components. s_{lq} (mol m^{-3}) is liquid water volume fraction in the pores. S_{lq} (mol m^{-3} s^{-1}) is the source term for liquid water, including water production, phase change, water back diffusion and electro-osmosis drag effect. Due to the assumption of uniform gas pressure distribution in the fuel cell, the flow velocity of gas mixture ($\vec{u}_g$) and liquid water ($\imath\vec{u}_g$) is zero. Since this work is a one-dimensional analytical model, the mass conservation equation of liquid water can be simplified and converted into a series of mass balance equations, as listed in Table 2.

The various transport processes are simplified into one-dimension (through-plane direction, normal to the membrane) to achieve high calculation efficiency and meanwhile keep the integrality of the major transport processes. In addition, the convective transport can be neglected because it is only significant along the in-plane direction caused by the strong cross flow. The mass balance equations for the liquid water are listed in Table 2. In the mass balance equations of liquid water, *c* (mol m^{-3}) means the superficial molar concentration of liquid water, for example, $c_{GDL-MPL,GDL}^{lq,ano}$ represents the superficial molar concentration of liquid water at the interface between GDL and MPL on the GDL side at anode. $N_{ano,lq}$ and $N_{cat,lq}$ (mol m^{-2} s^{-1}) are the mass flux through the cell components in the anode and cathode in the direction perpendicular to the membrane. δ_j (m) is the thickness of the cell component *j*, GDL, MPL and CL. The capillary diffusivity of liquid water, D_{lq}, is calculated with the effective permeability of liquid water (K_{lq}, m^2), capillary pressure (p_c, Pa), dynamic viscosity (μ_{lq}, kg m^{-1} s^{-1}) and the local liquid water volume fraction (s_{lq}) [39]:

$$D_{lq} = -\frac{K_{lq}}{\mu_{lq}}\frac{dp_c}{ds_{lq}} \tag{15}$$

$$K_{lq} = K_0 s_{lq}^4 \tag{16}$$

where K_0 (m^2) is the intrinsic permeability of liquid water, as given in Table 1. According to [40,41], the capillary pressure (p_c, Pa) is given as a function of liquid water surface tension coefficient (σ_{lq}, N m^{-1}), contact angle (θ, °), porosity (ε), permeability (K_0, m^2), and liquid water volume fraction (s_{lq}).

$$p_c = \begin{cases} \sigma_{lq}\cos\theta\left(\frac{\varepsilon}{K_0}\right)^{0.5}\left[1.42(1-s_{lq}) - 2.12(1-s_{lq})^2 + 1.26(1-s_{lq})^3\right] & \text{if } \theta < 90^\circ \\ \sigma_{lq}\cos\theta\left(\frac{\varepsilon}{K_0}\right)^{0.5}\left[1.42s_{lq} - 2.12s_{lq}^2 + 1.26s_{lq}^3\right] & \text{if } \theta > 90^\circ \end{cases} \tag{17}$$

In this study, both the gas and liquid pressures are assumed to be continuous at the interface and the gas pressure in the fuel cell is fixed as 1 atm, as a result, the capillary pressure is also continuous, which is also descripted in Fig. 1. Taking the MPL and GDL for example, the continuous capillary pressure condition across the interface can be expressed as

$$p_{c,GDL-MPL,MPL} = p_{c,GDL-MPL,GDL} \tag{18}$$

In order to achieve the liquid water saturation jump across the interface of the neighboring porous layers, two liquid water volume fractions, $s_{lq,GDL-MPL,MPL}$ and $s_{lq,GDL-MPL,GDL}$, are solved at the interface. Combining Eqs. (17) and (18), due to the different contact angle, porosity and permeability of the neighboring layers, the liquid water volume fraction ($s_{lq,GDL-MPL,MPL}$ and $s_{lq,GDL-MPL,GDL}$) or the superficial molar concentration of liquid water ($c_{GDL-MPL,GDL}^{lq}$ and $c_{GDL-MPL,MPL}^{lq}$) is discontinuous at the interface between the neighboring layers and liquid water saturation jump can be obtained:

$$s_{lq,GDL-MPL,MPL} \neq s_{lq,GDL-MPL,GDL} \text{ or } c_{GDL-MPL,GDL}^{lq} \neq c_{GDL-MPL,MPL}^{lq} \tag{19}$$

$s_{lq,GDL-MPL,MPL}$ and $s_{lq,GDL-MPL,GDL}$ are liquid water volume fractions at the interface of GDL and MPL on the MPL and GDL side, respectively.

$c^{lq}_{GDL-MPL,GDL}$ and $c^{lq}_{GDL-MPL,MPL}$ are superficial molar concentration at the interface of GDL and MPL on the MPL and GDL side, respectively. This calculation is also applied for all the interfaces of the porous components in the fuel cell.

In the mass balance equations of liquid water in anode CL and cathode CL, as listed in Table 2, M_{H_2O} (18×10^{-3} kg mol^{-1}) is the molar mass of water. Due to the consumption of water in the cathode electrochemical reaction, the liquid water may be not enough for some specific operating condition, which is also carefully discussed in our previous study [38]. Therefore, the total operating current density, I (A m^{-2}), should be separated into two sections, current density produced by consuming liquid water, $I_{cat,lq}$ (A m^{-2}) and current density produced by consuming water vapor (I-$I_{cat,lq}$). Actually, with the increasing of operating current density, the amount of water back diffusion from anode to cathode may no longer keep with the electro-osmosis drag effect and cathode water consumption rate. Under this condition, there is no liquid water in the cathode. On the other hand, if the amount of liquid water is enough for the cathode consumption, the $I_{cat,lq}$ should equal to the total current density I. The electro-osmotic drag coefficient, $n_{d,}$ is defined as [7]:

$$n_d = 0.183\lambda + 1.3 \tag{20}$$

λ is defined as water content in the alkaline membrane and can be obtained by Eq. (4). ρ_{w-a} and ρ_{w-c} (kg m^{-3}) are the average superficial mass density of liquid water in the CL of anode and cathode, respectively. The water diffusivity in the membrane is mainly related to the water content (λ) and the operating temperature (T, K):

$$D_m = \begin{cases} (0.0051\lambda \times T - 1.44\lambda) \times 10^{-10} & 0.0 \leqslant \lambda \leqslant 14.0 \\ \quad (-23.2404 + 4.513\lambda - 0.28926\lambda^2 + 0.006131\lambda^3) & \\ \times (T - 303.15) \times 10^{-10} & \\ -(79.826 + 17.928\lambda - 1.3329\lambda^2 + 0.03337\lambda^3) \times 10^{-10} & \\ \qquad\qquad 14.0 < \lambda \leqslant 19.0 & \\ \quad [(-41.916 + 0.00613\lambda^3) \times (T - 303.15) + 8.5139] & \\ \times 10^{-10} & \lambda > 19.0 \end{cases} \tag{21}$$

Combining the mass balance equations in Table 2 and the continuous capillary pressure at the interfaces, the liquid water distribution in different layers and liquid saturation jump at the interfaces can be obtained.

According to the assumptions, due to the 100% humidified gases at anode inlet under the base operating condition, as listed in Table 1, water produced in the anode CL is in liquid phase. There is no phase change between vapor and liquid water at anode. However, in this study, considering the characteristic of liquid water shortage at cathode, the cathode humidification through liquid water injection is applied for the cathode inlet in order to further improve the cathode performance. Therefore, the phase change may occur in the cathode, as shown in the mass balance equations for liquid water in Table 2. $S_{vap-lq,j}$ (mol m^{-3} s^{-1}) means the source terms of phase change between vapor and liquid water in the cell components j, and is defined as:

$$S_{vap-lq,j} \begin{cases} \gamma_{cond}\varepsilon_j(1 - s_{lq,j})\frac{(p_{vap} - p_{sat})}{RT} & \text{if } p_{vap} > p_{sat} \text{ condensation} \\ \gamma_{evap}\varepsilon_j s_{lq,j}\frac{(p_{vap} - p_{sat})}{RT} & \text{if } p_{vap} \leqslant p_{sat} \text{ evaporation} \end{cases} \tag{22}$$

in which γ_{cond} and γ_{evap} (s^{-1}) refer to the condensation and evaporation rate of water, respectively, p_{vap} and p_{sat} (Pa) represent the partial pressure and saturated pressure of water vapor.The mass conservation equations of gas species can be expressed as:

$$\nabla \cdot (\rho_g \vec{u}_g Y_i) = \nabla \cdot (\rho_g D_i^{eff} \nabla Y_i) + S_i, i = H_2, O_2, vapor \tag{23}$$

where ρ_g (kg m^{-3}) is the mass density of gas mixture. $\vec{u}_g$ (m s^{-1}) is the flow velocity of gas mixtures. As aforementioned, the gas pressure is evenly distributed in the fuel cell and fixed as 1 atm, therefore, the flow velocity of gases is zero. Y_i is the mass fraction of gas species i. D_i^{eff} (m^2 s^{-1}) is the effective diffusivity of gas species i. c_i (mol m^{-3}) is molar concentration of gas species i, S_i (mol m^{-3} s^{-1}) is the source term for gas species i, including gas consumption and phase change. In this study, H_2, O_2 (or air) and water vapor is taken into account and the mass conservation can be simplified into one-dimensional mass balance forms, as listed in Table 3.

In the mass balance equations for gas species, as shown in Table 3, c_k^i means gas molar concentration, and the superscript i (H_2, O_2 *and water vapor*) means the gas species, and for the subscript k (*ch, ch-GDL, GDL-MPL and MPL-CL*), *ch* means the center of the flow channel, and *ch-GDL, GDL-MPL and MPL-CL* mean the interface between flow channel and GDL, GDL and MPL, and MPL and CL, respectively. D_i denotes the intrinsic diffusivity of species i. $A_{ch\text{-}GDL}$ (m^2) is the area of the interface between flow channel and GDL. *Sh* is the Sherwood number (2.3) for the laminar flow in the flow channel [42]. Since the convection term of the gases is neglected in this study, the mass balance equation is corrected by using Sherwood number which means the ratio between convective mass transfer and mass diffusion. d_h (m) is the hydraulic diameter of the flow channel and L (m) and W (m) are the length and width of the flow channel. In this study, the gas concentration is considered being linearly distributed in every specific layer. The effective diffusion coefficient of gas species ($D_{i,j}^{eff}, i = H_2, O_2, vapor; j = GDL, MPL, CL$, m^2 s^{-1}) is calculated from the intrinsic diffusion coefficient ($D_{i,j}, i = H_2, O_2, vapor; j = GDL, MPL, CL$, m^2 s^{-1}) based on the Bruggeman correlation [33] considering the porosity and blockage of liquid water [43]:

$$D_{i,j} = \begin{cases} \text{for } H_2 \text{ and anode vapor} \\ 1.055 \times 10^{-4}(T/333.15)^{1.5}(101325/p)^{1.0} \\ \text{for } O_2 \\ 2.652 \times 10^{-5}(T/333.15)^{1.5}(101325/p)^{1.0} \\ \text{for cathode vapor} \\ 2.982 \times 10^{-5}(T/333.15)^{1.5}(101325/p)^{1.0} \end{cases} \tag{24}$$

$$D_{i,j}^{eff} = D_{i,j}\varepsilon_j^{1.5}(1 - s_{lq})^{1.5} \tag{25}$$

2.6. Boundary and initial conditions

In this study, the amount of liquid water in the flow channel is considered to be constant depending on the humidification at inlet and the electrochemical reaction in CL under specific operating conditions, because a short and straight flow channel is considered in this study. The concentration of gases at the inlet is defined as follows:

$$c_{inlet}^i = \frac{X_i p_{inlet}}{RT} \tag{26}$$

in which c_{inlet}^i (mol m^{-3}) means the molar concentration of gas species i, H_2, O_2, vapor, at the inlet. X_i refers to the volume fraction of gas species i in the gas mixtures. p_{inlet} (Pa) represents the inlet pressure. Considering the reactants consumption in the electrochemical reaction, the boundary condition can be expresses as:

$$c_{outlet}^i = c_{inlet}^i - \frac{(I/nF)A_{ch-GDL}\varepsilon_{GDL}}{V_{inlet}^{gas}A_{inlet}} \tag{27}$$

c_{outlet}^i (mol m^{-3}) is the molar concentration of gas species i, H_2, O_2, vapor, at the outlet. A_{ch-GDL} is the area of the interface between flow

channel and GDL. ε_{GDL} is the porosity of GDL. V_{inlet}^{gas} (m s^{-1}) is the flow velocity of gas mixtures. A_{inlet} (m^{-2}) is the inlet area of the flow channel.

$$V_{inlet}^{gas} = \frac{(I/nF)A_{act}ST}{A_{inlet}c_{inlet}^{i}} \tag{28}$$

A_{act} (m^2) is the active area in the CL. ST is the stoichiometry ratio. Therefore, the average molar concentration of gas species i in the flow channel can be calculated by assuming a linear relationship:

$$c_{ch}^{i} = \frac{c_{inlet}^{i} + c_{outlet}^{i}}{2} \tag{29}$$

2.7. Comparison to experimental data

A schematic of the experimental setup is shown in Fig. 1b. The cell is placed in an environmental chamber and humidified hydrogen and air are supplied to the AEMFC. The environmental chamber and the inlet flow are set to have the same temperature which is regarded as the operating temperature during the tests. The AEMFC has a serpentine flow field with cross sectional dimensions of 1 mm by 1 mm and the active area of 5 cm by 5 cm. The membrane electrode assembly (MEA) is consisted of A201 membrane, Pt/C catalysts and GDL with MPL. A catalyst coated membrane (CCM) was fabricated by spraying the catalyst ink on the A201 membrane under infrared spotlight. The Pt catalyst loading is 0.5 mg cm^{-2} for both the anode and cathode. The thickness of the GDL (carbon paper) with MPL is 230 μm. The weight fraction of ionomer in the CL is 30.01%. The experimental cell design parameters and operating conditions are listed in Table 4. The polarization curve (I-V curve) is tested in constant voltage mode. The OCV-0.1 V-OCV means that the testing process of I-V curve is from open circuit voltage (OCV) to 0.1 V, and back to OCV.

The numerical simulation is based on the same operating conditions and parameters as summarized in Table 1 and the results are compared with experimental data in Fig. 2. Fig. 2a shows the comparison with the present experimental results. The operating temperature was set as 50 °C. The anode inlet was supplied by the hydrogen with 100% relative humidity and the cathode by the oxygen with two different humidification conditions, 90% and 100%, for results comparison. Experimental results in Fig. 2b is from Kruusenberg et al. [11], in which the operating temperature was 45 °C and the anode and cathode were supplied by fully humidified hydrogen and air, respectively. The modeling predicted I-V curves represent reasonable agreements with experimental data for both cases as shown in Fig. 2a and b.

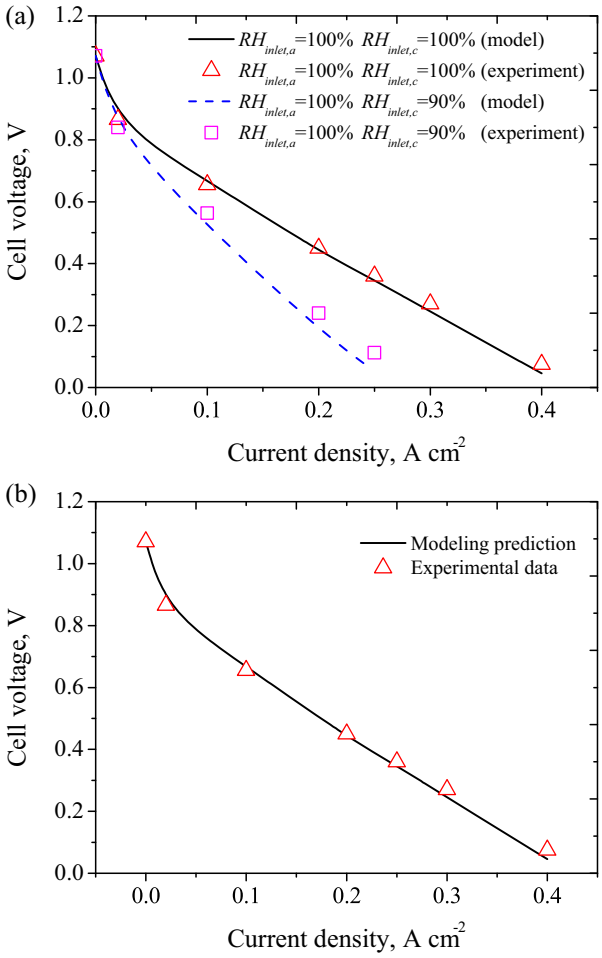

Fig. 2. Comparison between the present model predictions and experimental cell test data (a) comparison with present experimental study, (b) comparison with Kruusenberg et al. [11].

Table 4
Cell design parameters and operating conditions for the experimental test.

Cell design parameters	
Cell components	Values
Pt catalyst loading (anode)	0.5 mg cm^{-2}
Pt catalyst loading (cathode)	0.5 mg cm^{-2}
Alkaline exchange membrane	Membrane: A201 (active area: 5 cm × 5 cm) Thickness: 28 μm IEC: 1.8 mmol g^{-1} Electrical conductivity: 42 mS cm^{-1}
GDL H2415 (Freudenberg Germany)	Thickness: 230 μm Permeability: 35 s (ISO 5636-5)
Operating conditions	
Parameters	Values
Cell voltage	OCV - 0.1 V – OCV (constant voltage mode)
Anode gas	H_2
Cathode gas	Air
Relative humidity of anode inlet gas	100%
Relative humidity of cathode inlet gas	100% and 90%
Environment temperature	40 °C
Inlet temperature	50 °C
Anode inlet flow rate	0.5 slpm
Cathode inlet flow rate	1.0 slpm
Activation voltage	0.1 V

3. Results and discussion

3.1. Effect of cathode CL contact angle

In an AEMFC, the activation energy of the cathode half-reaction is much larger than that of the anode, and as such, sluggish cathode reaction kinetic is considered the dominating factor in dragging performance. Since the water is consumed in the cathode, the cathode CL wettability has significant impact on the performance of AEMFC. To investigate the effect of the cathode CL contact angle on the cell performance, the numerical simulation has been performed for different cathode CL contact angles including both the hydrophilic (contact angle: 80° and 85°) and hydrophobic cathode CLs (contact angle: 95°, 100° and 110°). The stoichiometry is set as 2.0 and the relative humidity is maintained at 100% for the inlets of the anode and cathode. The cell is running at constant temperature and pressure of 50 °C and 1 atm, respectively. The MPL is not

considered in this section in order to specifically investigate the effect of CL contact angles on the cell performance.

Fig. 3a shows the voltage and power density of the cell for different CL contact angles. The voltage and power density increase as the cathode CL contact angle decreases, i.e. becomes more hydrophilic. This is attributed to the fact that the activation and ohmic overpotentials decrease as the cathode CL becomes more hydrophilic, as shown in Fig. 3b. Since the cathode electrochemical reaction consumes water, a less hydrophobic cathode CL can attract and retain more water which results in a higher membrane conductivity. The relative humidity in cathode CL is also higher for the lower contact angles as shown in Fig. 4. At a low current density, the relative humidity was maintained high regardless the contact angle balanced by the back diffusion of water from the anode. However, the relative humidity rapidly decreases as the current density increases due to the water consumption and electro-osmotic drag. This phenomenon is more apparent for larger cathode CL contact angles, since the hydrophobic CL hinders back diffusion of water from the anode. For the anode electrochemical reaction, due to the low limiting current density of AEMFC, the anode is not completely flooded.

3.2. Effect of cathode humidification

Since the cathode reaction takes water proper humidification is also critical to prevent cathode dehydration and thus to improve the performance. In this section, the effect of the cathode humidification has been investigated. The cathode CL contact angle is fixed as 100° and other operating conditions remain the same as previous section. Hydrophobic cathode CL is considered common for the polymer electrolyte membrane fuel cells and widely used in the modeling work [35,44,45].

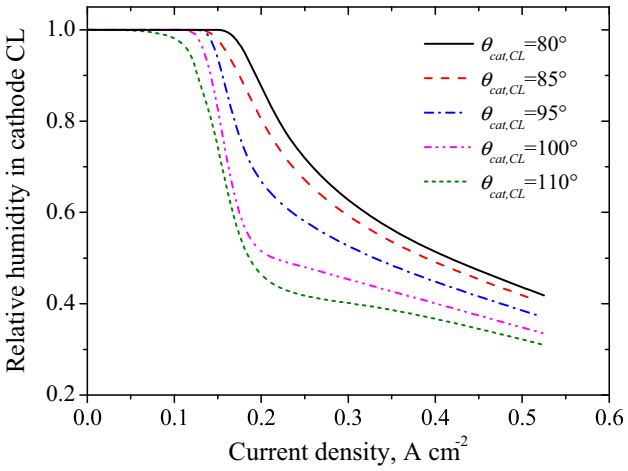

Fig. 4. Relative humidity in the cathode CL for different contact angles of cathode CL ($\theta_{cat,CL}$).

Fig. 5a shows cell voltage and power density for different cathode inlet humidity conditions. The liquid water injection with the volume fraction of 0.2 is also considered in this study. The averaged liquid water concentration in the flow channel is determined based on the rate of consumption at the cathode CL and the liquid water transport from the flow channel to the cathode CL is assumed to be driven by diffusion. Fig. 5 shows that the performance dramatically improves according to increasing cathode inlet humidity. With the aid of liquid water injection, the peak power

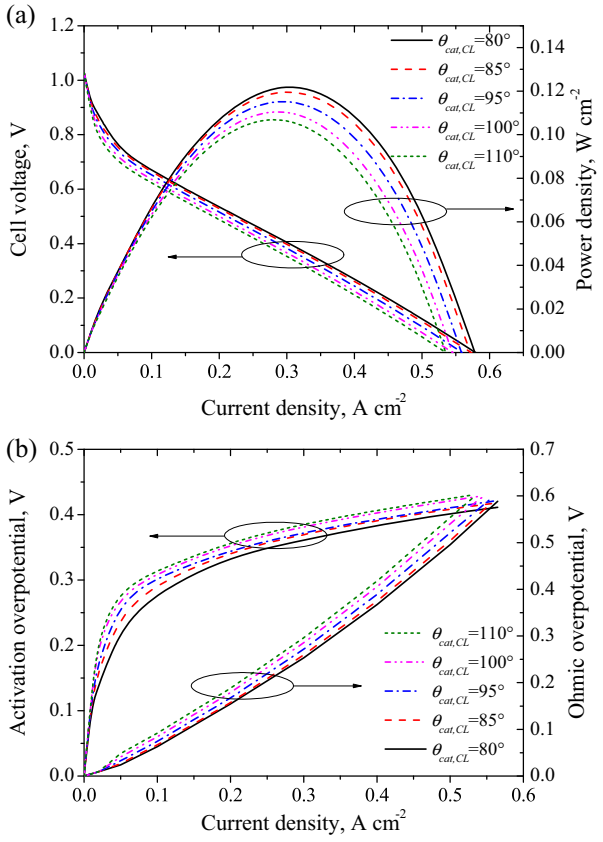

Fig. 3. Effect of cathode CL contact angles ($\theta_{cat,CL}$) on (a) cell voltage (V) and power density (W cm^{-2}), (b) activation and ohmic overpotential (V).

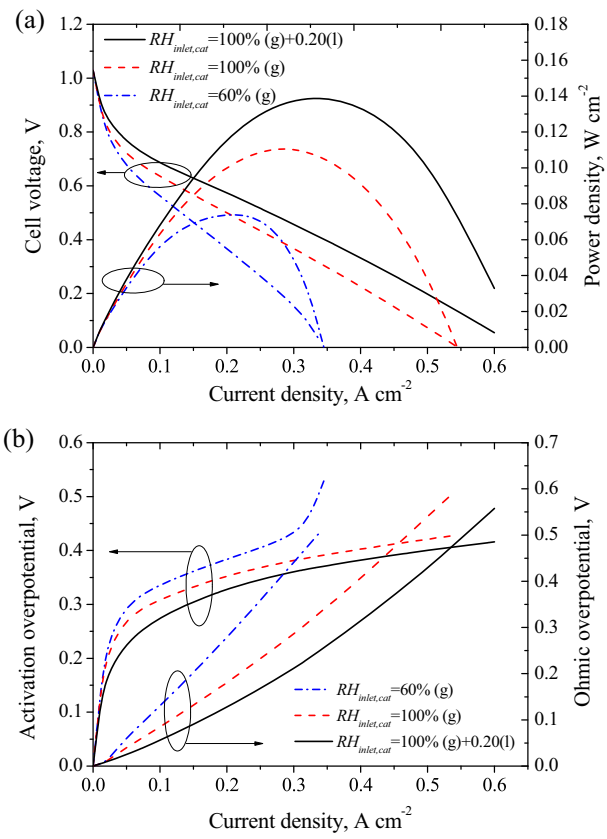

Fig. 5. Effect of cathode inlet humidity conditions ($RH_{inlet,\ cat}$) on (a) cell voltage (V) and power density (W cm^{-2}), (b) activation and ohmic overpotential (V).

density is increased by 100% when compared to the relative humidity of 60%. As shown in Fig. 5b, the cathode overpotentials, especially the ohmic overpotential, significantly reduce with increasing water support. This is mainly caused by enhanced conductivity of the membrane since the effect of water content on ohmic resistances of other cell components are negligible. The electrical conductivity of the membrane is determined in terms of cell temperature and water activity according to Eq. (6). The liquid water injection has great potential to improve the performance of AEMFC, however it may cause flooding in the flow channel and GDL. This idea will require experimental verifications. Although not shown, the relative humidity of the anode inlet has no significant effect on the performance due to the intrinsic water flooding conditions for the anode. However, the relative humidity at anode inlet may affect the cell performance under unsteady or dynamic operating conditions, such as starting-up processes, due to its humidification function for the alkaline membrane.

3.3. Effect of the MPLs

As aforementioned, MPL has been considered as an effective way to improve the water transport behaviors, as well as the reactant feeding for the traditional PEMFC. Therefore, in this study, the MPL is taken into account. The MPL is regarded as hydrophobic with the contact angle of 100°. The inlet humidity was set as 100% on both the cathode and anode sides.

Fig. 6a shows the cell voltage and power density for different MPL configurations. It is shown that the effect of the anode MPL is positive on performance, however that of the cathode MPL is not. This is attributed to the fact that the reduced water transport across the MPL has different effects in the anode and cathode. In anode, the MPL hinders the water transport from anode CL to GDL, increasing water content in CL. This, in turn, promotes the back diffusion of water from the anode to cathode. In cathode, however, the MPL hinders water transport from cathode flow channel to CL, decreasing the water content. This has a significant influence on both the activation and ohmic overpotential. As a result, the MPL in the anode only shows the best performance, while the MPL in the cathode presents the worst performance; even lower than with no MPL configuration. It is noted that the voltage of cell with cathode MPL is higher than that with no MPL when the current density is lower than 0.05 A cm^{-2}. This may be

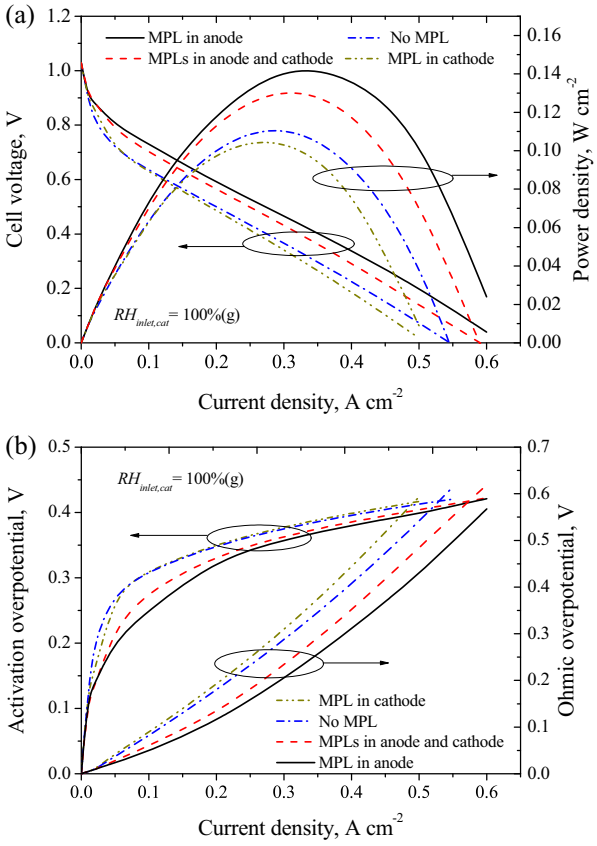

Fig. 6. Effect of MPL configurations on (a) cell voltage (V) and power density (W cm^{-2}), (b) activation and ohmic overpotential (V) with 100% cathode inlet humidification.

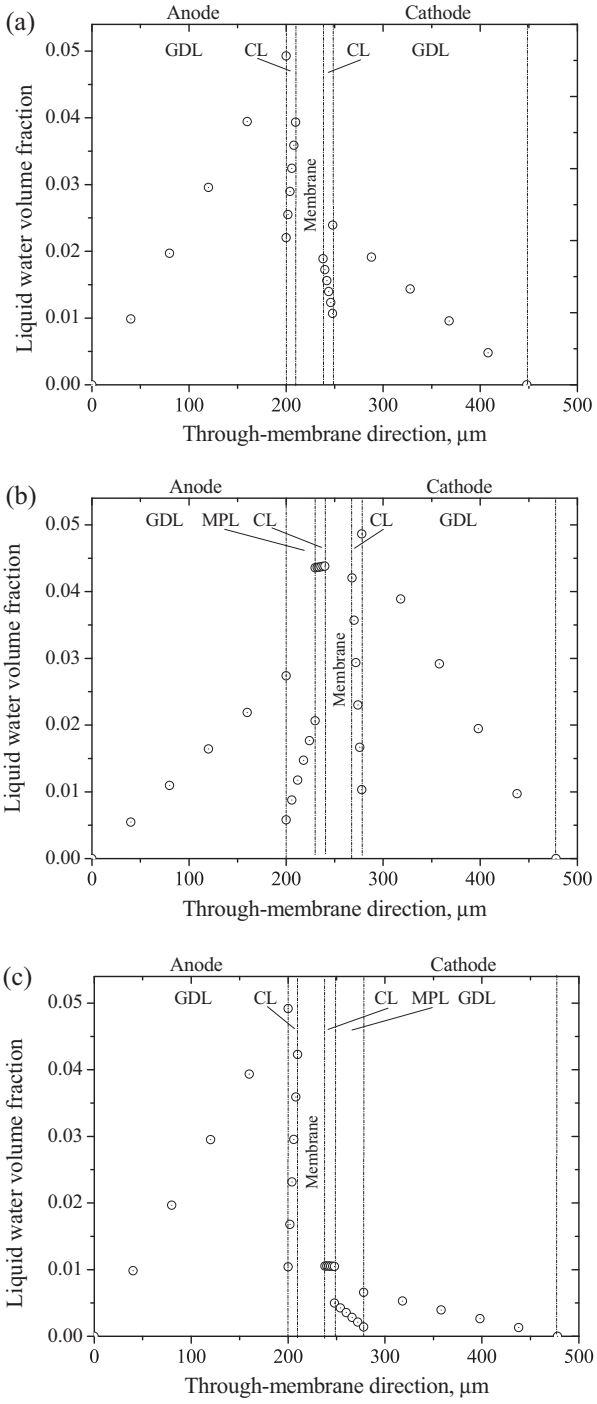

Fig. 7. Liquid water distributions in the cell components with 100% cathode inlet humidification under 0.1 A cm^{-2}: (a) with no MPL, (b) with MPL in anode, and (c) with MPL in cathode.

attributed to the fact that back diffusion is dominant to the electro-osmotic drag at low current densities.

Fig. 7 shows the liquid water distribution in the cell components for the three different MPL configurations, (a) no MPL, (b) MPL in anode and (c) MPL in cathode, when current density is 0.1 A cm^{-2}. Moreover, it should be noticed that liquid saturation jumps at the interfaces of neighboring layers occur, as displayed in Fig. 7. As mentioned previously, the calculation of liquid saturation jump is based on the continuous liquid pressure or capillary pressure, as descript in Eq. (18). Fig. 7a indicates that average liquid water content in the CL and GDL is much higher in anode than that in cathode when no MPL is implemented. However, the anode MPL significantly aids in raising the liquid water content in cathode CL and GDL as shown in Fig. 7b. Moreover, Anode MPL slows the liquid water flow in the anode and promotes the liquid water flow in the cathode, as shown in Fig. 7a and b, enhancing the water back diffusion to the cathode CL, which leads to significant liquid saturation jump at cathode. On the other hand, the effect of the cathode MPL is negative, as it blocks the water vapor support from the cathode channel, thus leading to the lowest amount water in the cathode among three MPL configurations. In addition, the liquid water in cathode CL comes from the anode, which needs to be removed through the cathode flow channel. With the insertion of cathode MPL, the total water flux from anode CL to cathode flow channel is reduced, leading to less water in cathode CL. Although the anode MPL may promote water accumulation, the relatively high liquid water content in the anode CL would lead to a significant increment of the water content in cathode CL, in turn resulting in faster cathode reaction kinetics. Overall, to achieve optimal cell performance, the MPL is suggested to be used only at the anode side, with proper humidification at the cathode inlet.

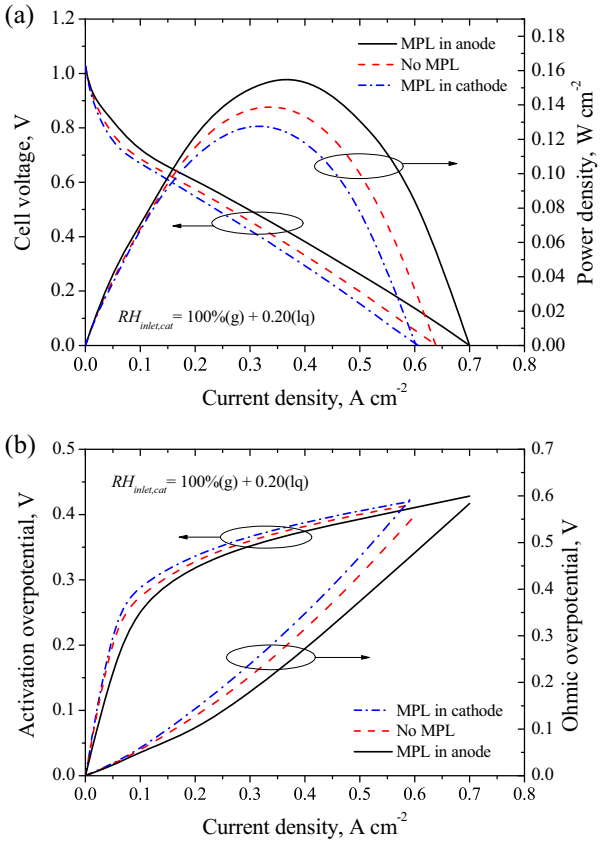

Fig. 8. Effect of MPL configurations on (a) cell voltage (V) and power density (W cm^{-2}), (b) activation and ohmic overpotential (V) with 100% cathode inlet humidification and extra liquid water injection of 0.20 volume fraction.

In order to further investigate the performance dependence of AEMFC on the water transfer behavior, extra liquid water injection for the cathode inlet humidification is implemented in this study. Fig. 8 depicts the cell performance with 100% cathode inlet humidification by vapor and extra liquid water injection of 0.2 volume fraction. It is obvious that by supplying more water for the cathode, the cell performance raises up greatly. For instance, the limiting current density for the three MPL cases pulls up for 0.1 A cm^{-2}

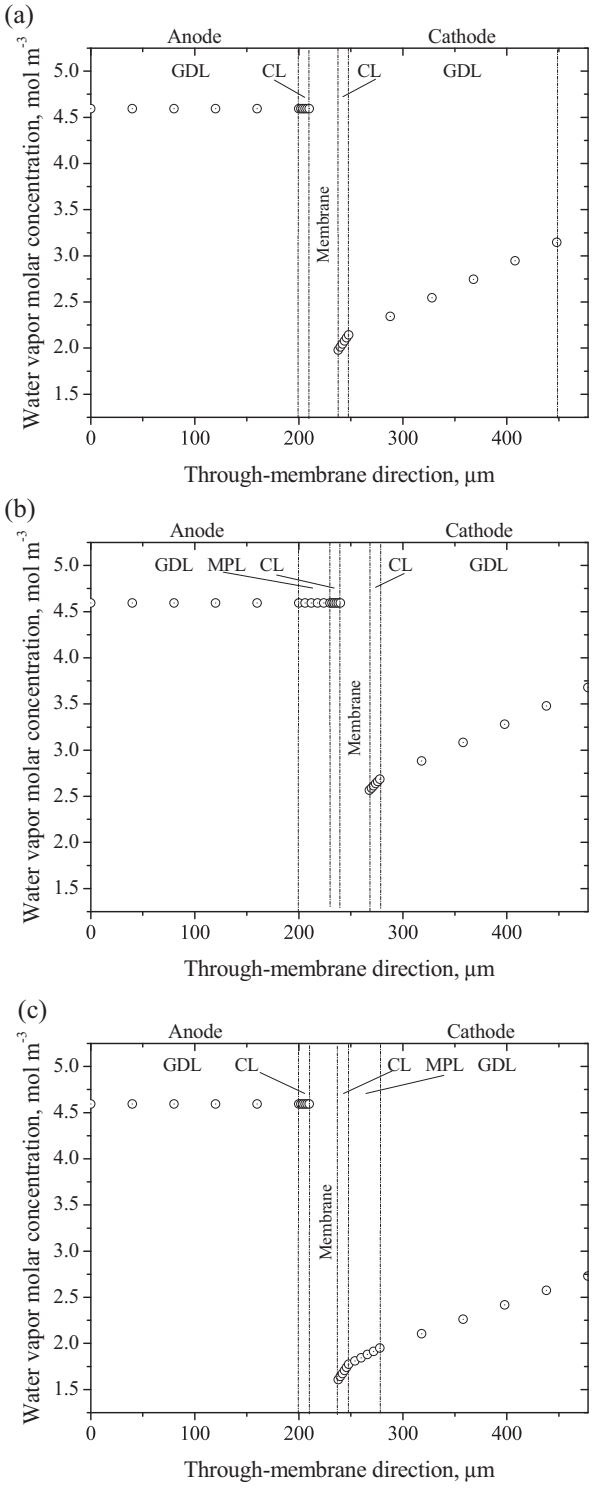

Fig. 9. Water vapor distributions in the cathode with 100% cathode inlet humidification and extra liquid water injection of 0.20 volume fraction under 0.5 A cm^{-2}: (a) with no MPL, (b) with MPL in anode, and (c) with MPL in cathode.

approximately. It should be noted that although the liquid water is fed for the cathode, the liquid water reactant is found not enough for the electrochemical reaction. The liquid water is consumed out at around 0.140, 0.195, 0.120 A cm^{-2} for the No MPL case, MPL in anode case and MPL in cathode case, respectively, hence as current density increases, water vapor starts being the main reactant for the cathode reaction. Therefore, the cell performance under higher current densities should be dominated by the water vapor transfer behaviors. It should be noted that the hydrophobic MPL just slows down the transfer rate of liquid water from cathode flow channel into CL, not completely stops the liquid water transport across the MPL.

Fig. 9 shows the water vapor molar concentration distribution in the cell components. The water vapor concentration is the lowest for the cathode MPL case due to the retardant function of MPL for the vapor feeding, rigorous consumption in the reaction and weaker liquid water supply. The cathode MPL slows the liquid water transport into the CL, resulting in the less liquid water consumption and more vapor consumption in the CL. It further results in larger concentration gradient of water vapor from the flow channel into the GDL. To maintain sufficient membrane hydration and effective cathode reactant supplement, sufficient humidification of cathode and proper MPL assembly is crucial for the cell output which can be improved by liquid injection, and if the feeding cathode gases only contain water vapor, high reactant flow rate may be required.

4. Conclusion

In this study, an analytical model for hydrogen alkaline anion exchange membrane fuel cell (AEMFC) has been formulated to investigate the electrode wettability effect on the water transport and polarization characteristics. The liquid saturation jump on the interfaces of the neighboring components is also modeled. It is found that the cathode catalyst layer (CL), contact angle, cathode humidification and the micro-porous layer (MPL) have significant impacts on the performance of the AEMFC due to their effects on the water transfer behavior. Considering the electro-osmosis drag and the consumption in the electrochemical reaction, water is consumed much faster than oxygen (O_2) in the cathode CL, which indicates that the membrane hydration on the cathode side needs special attention. Decreasing the cathode CL contact angle (more hydrophilic) generally improves the performance by retaining more water close to the membrane, especially at high current densities. Liquid water injection into the cathode can further improve the cell performance however may cause flooding. The anode MPL is useful in improving the performance by forcing more water to diffuse back to the cathode. However the MPL is suggested to be implemented only in the anode since the cathode MPL hinders water transport from the gas diffusion layer (GDL) to CL resulting in dehydration. Therefore, in order to maintain sufficient membrane hydration and effective cathode reactant supplement, sufficient humidification of cathode and proper MPL assembly should be regarded as a critical issue for AEMFC operation, which may require further humidification by liquid water injection and high reactant flow rate.

Acknowledgements

This work was supported by the National Natural Science Foundation of China for Excellent Young Scholars (Grant No. 51622606), and the Key Program of Natural Science Foundation of Tianjin (China) (Grant No. 16JCZDJC30800).

References

[1] Z. Wan, J. Shen, H. Zhang, Z. Tu, W. Liu, In situ temperature measurement in a 5 kW-class Proton Exchange Membrane Fuel Cell stack with pure oxygen as the oxidant, Int. J. Heat Mass Transfer 75 (2014) 231–234.
[2] L. Chen, Y.-L. Feng, C.-X. Song, L. Chen, Y.-L. He, W.-Q. Tao, Multi-scale modeling of proton exchange membrane fuel cell by coupling finite volume method and lattice Boltzmann method, Int. J. Heat Mass Transfer 63 (2013) 268–283.
[3] A. Faghri, Z. Guo, Challenges and opportunities of thermal management issues related to fuel cell technology and modeling, Int. J. Heat Mass Transfer 48 (19–20) (2005) 3891–3920.
[4] N. Sulaiman, M.A. Hannan, A. Mohamed, E.H. Majlan, W.R. Wan Daud, A review on energy management system for fuel cell hybrid electric vehicle: issues and challenges, Renew. Sust. Energy Rev. 52 (2015) 802–814.
[5] I. Verhaert, G. Mulder, M.D. Paepe, Evaluation of an alkaline fuel cell system as a micro-CHP, Energy Convers. Manage. 126 (2016) 434–445.
[6] S. Markgraf, M. Hörenz, T. Schmiel, W. Jehle, J. Lucas, N. Henn, Alkaline fuel cells running at elevated temperature for regenerative fuel cell system applications in spacecrafts, J. Power Sources 201 (2012) 236–242.
[7] Y.S. Li, T.S. Zhao, W.W. Yang, Measurements of water uptake and transport properties in anion-exchange membranes, Int. J. Hydrogen Energy 35 (11) (2010) 5656–5665.
[8] Q. Duan, S. Ge, C.-Y. Wang, Water uptake, ionic conductivity and swelling properties of anion-exchange membrane, J. Power Sources 243 (2013) 773–778.
[9] C.M. Tuan, D. Kim, Anion-exchange membranes based on poly (arylene ether ketone) with pendant quaternary ammonium groups for alkaline fuel cell application, J. Membr. Sci. 511 (2016) 143–150.
[10] B. Lin, F. Chu, Y. Ren, B. Jia, N. Yuan, H. Shang, T. Feng, Y. Zhu, J. Ding, Alkaline stable C2-substituted imidazolium-based cross-linked anion exchange membranes for alkaline fuel cell applications, J. Power Sources 266 (2014) 186–192.
[11] I. Kruusenberg, L. Matisen, Q. Shah, A.M. Kanan, K. Tammeveski, Non-platinum cathode catalysts for alkaline membrane fuel cells, Int. J. Hydrogen Energy 37 (5) (2012) 4406–4412.
[12] X. Li, B.N. Popov, T. Kawahara, H. Yanagi, Non-precious metal catalysts synthesized from precursors of carbon, nitrogen, and transition metal for oxygen reduction in alkaline fuel cells, J. Power Sources 196 (4) (2011) 1717–1722.
[13] M. Alesker, M. Page, M. Shviro, Y. Paska, G. Gershinsky, D.R. Dekel, D. Zitoun, Palladium/nickel bifunctional electrocatalyst for hydrogen oxidation reaction in alkaline membrane fuel cell, J. Power Sources 304 (2016) 332–339.
[14] H.-Y. Park, S.H. Park, M.S. Park, H.-J. Kim, D. Henkensmeier, S.J. Yoo, J.Y. Kim, J. H. Ryu, J.H. Jang, Development of $La_{0.8}Sr_{0.2}MnO_{3+\delta}$ electrocatalysts by Pechini's methods as cathode electrocatalysts in alkaline anion exchange membrane fuel cells, Solid State Ionics 290 (2016) 124–129.
[15] N.W. Lee, S.I. Kim, Y.S. Kim, S.H. Kim, B.K. Ahn, M.S. Kim, An effective discharge method for condensed water inside the GDL using pressure gradient of a PEM fuel cell, Int. J. Heat Mass Transfer 85 (2015) 703–710.
[16] J.P. Owejan, T.A. Trabold, M.M. Mench, Oxygen transport resistance correlated to liquid water saturation in the gas diffusion layer of PEM fuel cells, Int. J. Heat Mass Transfer 71 (2014) 585–592.
[17] S. Huo, H. Deng, Y. Chang, K. Jiao, Water management in alkaline anion exchange membrane fuel cell anode, Int. J. Hydrogen Energy 37 (23) (2012) 18389–18402.
[18] H. Deng, S. Huo, Y. Chang, Y. Zhou, K. Jiao, Transient analysis of alkaline anion exchange membrane fuel cell anode, Int. J. Hydrogen Energy 38 (15) (2013) 6509–6525.
[19] H. Deng, J. Chen, K. Jiao, X. Huang, An analytical model for alkaline membrane direct methanol fuel cell, Int. J. Heat Mass Transfer 74 (2014) 376–390.
[20] H. Deng, D. Jiao, M. Zu, J. Chen, K. Jiao, X. Huang, Modeling of passive alkaline membrane direct methanol fuel cell, Electrochim. Acta 154 (2015) 430–446.
[21] K. Jiao, P. He, Q. Du, Y. Yin, Three-dimensional multiphase modeling of alkaline anion exchange membrane fuel cell, Int. J. Hydrogen Energy 39 (11) (2014) 5981–5995.
[22] I.P. Raya, M.W. Ellis, A. Hernandez-Guerrero, F. Elizalde-Blancas, Modeling the effect of membrane conductivity on the performance of alkaline fuel cells, J. Power Sources 307 (2016) 898–906.
[23] C. Weinzierl, U. Krewer, Model-based analysis of water management at anode of alkaline direct methanol fuel cells, Chem. Eng. Sci. 143 (2016) 181–193.
[24] S. Abdullah, S.K. Kamarudin, U.A. Hasran, M.S. Masdar, W.R.W. Daud, Electrochemical kinetic and mass transfer model for direct ethanol alkaline fuel cell (DEAFC), J. Power Sources 320 (2016) 111–119.
[25] P.S. Khadke, U. Krewer, Performance losses at H_2/O_2 alkaline membrane fuel cell, Electrochem. Commun. 51 (2015) 117–120.
[26] D.-D. Ye, B. Zhang, X. Zhu, P.-C. Sui, N. Djilali, Q. Liao, Computational modeling of alkaline air-breathing microfluidic fuel cells with an array of cylinder anodes, J. Power Sources 228 (2015) 150–159.
[27] N. Ge, S. Chevalier, J. Lee, R. Yip, R. Banerjee, M.G. George, H. Liu, C.H. Lee, M. Fazeli, P. Antonacci, T. Kotaka, Y. Tabuchi, A. Bazylak, Non-isothermal two-phase transport in a polymer electrolyte membrane fuel cell with crack-free microporous layers, Int. J. Heat Mass Transfer 107 (2017) 418–431.

[28] R. Banerjee, A. Bazylak, Modeling heat transfer through phase-differentiated nano-scale constructions of polymer electrolyte membrane fuel cell microporous layers, Int. J. Heat Mass Transfer 92 (2016) 131–138.
[29] J.H. Nam, K.-J. Lee, G.-S. Hwang, C.-J. Kim, M. Kaviany, Microporous layer for water morphology control in PEMFC, Int. J. Heat Mass Transfer 52 (11–12) (2009) 2779–2791.
[30] G. Chen, G. Zhang, L. Guo, H. Liu, Systematic study on the functions and mechanisms of micro porous layer on water transport in proton exchange membrane fuel cells, Int. J. Hydrogen Energy 41 (9) (2016) 5063–5073.
[31] Y. Tabe, Y. Aoyama, K. Kadowaki, K. Suzuki, T. Chikahisa, Impact of micro-porous layer on liquid water distribution at the catalyst layer interface and cell performance in a polymer electrolyte membrane fuel cell, J. Power Sources 287 (2015) 422–430.
[32] R. O'Hayre, S. Che, W. Collera, F.B. Priz, Fuel Cell Fundamentals, John Wiley & Sons, New York, 2006.
[33] D.A.G. Bruggeman, The calculation of various physical constants of heterogeneous substances. I. The dielectric constants and conductivities of mixtures composed of isotopic substances, Ann. Phys. 24 (1935) 636–664.
[34] T.E. Springer, T.A. Zawodzinski, S. Gottesfeld, Polymer electrolyte fuel cell model, J. Electrochem. Soc. 138 (8) (1991) 2334–2342.
[35] K. Jiao, X. Li, Water transport in polymer electrolyte membrane fuel cells, Prog. Energy Combust. 37 (3) (2011) 221–291.
[36] T.A. Zawodzinski, T.E. Springer, J. Davey, R. Jestel, C. Lopez, J. Valerio, S. Gottesfeld, A comparative study of water uptake by and transport through ionomeric fuel cell membranes, J. Electrochem. Soc. 140 (7) (1993) 1981–1985.
[37] T.A. Zawodzinski, C. Derouin, S. Radzinski, R.J. Sherman, V.T. Smith, T.E. Springer, S. Gottesfeld, Water uptake by and transport through Nafion 117 membranes, J. Electrochem. Soc. 140 (4) (1993) 1041–1047.
[38] K. Jiao, S. Huo, M. Zu, D. Jiao, J. Chen, Q. Du, An analytical model for hydrogen alkaline anion exchange membrane fuel cell, Int. J. Hydrogen Energy 40 (8) (2015) 3300–3312.
[39] Q. Ye, T.V. Nguyen, Three dimensional simulation of liquid water distribution in a PEMFC with experimentally measured capillary functions, J. Electrochem. Soc. 154 (12) (2007) B1242–B1251.
[40] F.A.L. Dullien, Porous Media: Fluid Transport and Pore Structure, second ed., Academic Press, San Diego, 1992.
[41] K.S. Udell, Heat transfer in porous media considering phase change and capillarity-the heat pipe effect, Int. J. Heat Mass Transfer 28 (2) (1985) 485–495.
[42] P.K. Das, X. Li, Z.-S. Liu, Analytical approach to polymer electrolyte membrane fuel cell performance and optimization, J. Electroanal. Chem. 604 (2) (2007) 72–90.
[43] D. Natarajan, T.V. Nguyen, Three-dimensional effects of liquid water flooding in the cathode of a PEM fuel cell, J. Power Sources 115 (1) (2003) 66–80.
[44] W.W. Yang, M.Y. Lu, Y.L. He, Performance study of an alkaline direct ethanol fuel cell with a reduced two-dimensional mass transport model, Int. J. Hydrogen Energy 41 (2016) 20693–20708.
[45] T. Bednarek, G. Tsotridis, Issues associated with modelling of proton exchange membrane fuel cell by computational fluid dynamics, J. Power Sources 343 (2017) 550–563.